

PHYSICS CONTRIBUTION

INVERSE TREATMENT PLANNING BASED ON MRI FOR HDR PROSTATE BRACHYTHERAPY

DEBORAH CITRIN, M.D.,* HOLLY NING, PH.D.,* PETER GUION, M.S.,* GUANG LI, PH.D.,*
ROBERT C. SUSIL, PH.D.,† ROBERT W. MILLER, PH.D.,* ETIENNE LESSARD, PH.D.,‡
JEAN POULIOT, PH.D.,‡ XIE HUCHEN, PH.D.,* JACEK CAPALA, PH.D.,* C. NORMAN COLEMAN, M.D.,*
KEVIN CAMPHAUSEN, M.D.,* AND CYNTHIA MÉNARD, M.D.*

*Radiation Oncology Branch, CCR, National Cancer Institute, National Institutes of Health, Department of Health and Human Services, Bethesda, MD; †Department of Biomedical Engineering, Johns Hopkins University School of Medicine, Baltimore, MD; ‡Department of Radiation Oncology, University of California, San Francisco, San Francisco, CA

Purpose: To develop and optimize a technique for inverse treatment planning based solely on magnetic resonance imaging (MRI) during high-dose-rate brachytherapy for prostate cancer.

Methods and Materials: Phantom studies were performed to verify the spatial integrity of treatment planning based on MRI. Data were evaluated from 10 patients with clinically localized prostate cancer who had undergone two high-dose-rate prostate brachytherapy boosts under MRI guidance before and after pelvic radiotherapy. Treatment planning MRI scans were systematically evaluated to derive a class solution for inverse planning constraints that would reproducibly result in acceptable target and normal tissue dosimetry.

Results: We verified the spatial integrity of MRI for treatment planning. MRI anatomic evaluation revealed no significant displacement of the prostate in the left lateral decubitus position, a mean distance of 14.47 mm from the prostatic apex to the penile bulb, and clear demarcation of the neurovascular bundles on postcontrast imaging. Derivation of a class solution for inverse planning constraints resulted in a mean target volume receiving 100% of the prescribed dose of 95.69%, while maintaining a rectal volume receiving 75% of the prescribed dose of <5% (mean 1.36%) and urethral volume receiving 125% of the prescribed dose of <2% (mean 0.54%).

Conclusion: Systematic evaluation of image spatial integrity, delineation uncertainty, and inverse planning constraints in our procedure reduced uncertainty in planning and treatment. © 2005 Elsevier Inc.

Brachytherapy, High dose rate, Inverse planning, MRI, Prostate.

INTRODUCTION

The ability to provide superior visualization of the prostate gland and surrounding anatomy makes magnetic resonance imaging (MRI) the modality of choice for imaging prostate cancer. Endorectal coil MRI of the prostate gland has clearly demonstrated value for staging and prognostication in patients with localized disease (1–8). When combined with biologic imaging techniques, such as spectroscopic MRI (9–11) and dynamic contrast-enhanced MRI (12), it holds promise for accurate localization of the intraprostatic tumor burden.

Magnetic resonance imaging has been used to supplement other imaging techniques in the planning of external beam radiotherapy (13, 14). The basis for the application of MRI in external beam radiotherapy is an improved ability to define the target volume accurately (15). Avoidance of

neurovascular and erectile tissue with external beam radiotherapy using co-registered MRI-based anatomic delineation has been reported (16, 17).

Given that accuracy in brachytherapy is largely dependent on the planning image quality, the rationale is strong for using MRI for the treatment planning of brachytherapy. MRI has recently been used to plan and evaluate the quality of prostate brachytherapy procedures (18–22). Alterations in patient selection for prostate brachytherapy and modifications of planned source distribution to treat areas of extraprostatic extension on the basis of endorectal MRI findings have been reported (21). Low-dose-rate and high-dose-rate (HDR) brachytherapy dose escalation of preplanning spectroscopic MRI-defined intraprostatic lesions has also recently been described (20, 22). However, all studies published to date have relied on deformable registration of diagnostic MRI scans with ultrasound or computed tomog-

Reprint requests to: Deborah Citrin, M.D., Radiation Oncology Branch, NCI, Bldg. 10, Rm. B3B69, 9000 Rockville Pike, Bethesda, MD 20892. Tel: (301) 496-5457; Fax: (301) 480-5438; E-mail: citrind@mail.nih.gov

Work in research collaboration with Nucletron Inc.

Acknowledgments—Special thanks to Dr. Paul Albert for his assistance with the statistics.

Received Jul 30, 2004, and in revised form Nov 10, 2004. Accepted for publication Nov 17, 2004.

raphy (CT) image sets, with the potential of introducing registration error.

In the context of MRI-based planning, HDR temporary implants may offer an advantage whereby complex dose distributions can be achieved by optimizing dwell times after catheter placement. D'Amico and colleagues (23) reported low-dose-rate brachytherapy performed with real-time MRI guidance. Preliminary reports of treatment planning for HDR prostate brachytherapy using MRI have been recently reported (20).

We previously described our initial clinical experience with a novel MRI-guided HDR prostate brachytherapy procedure performed in a high-field cylindrical 1.5T scanner (24, 25). Here, we further describe five steps for implementation of inverse treatment planning based and guided solely by MRI for HDR prostate brachytherapy. These steps include (1) correction and verification of spatial distortion in MRI; (2) Digital Imaging and Communications in Medicine interface (DICOM) header correction for compliance to the treatment planning software; (3) validation of a technique for determination of the first dwell position; (4) anatomic evaluation based on MRI; and (5) derivation of optimal inverse planning constraints.

METHODS AND MATERIALS

MRI-guided brachytherapy procedure

Ten patients with intermediate- and high-risk clinically localized prostate cancer provided informed consent for enrollment in an institutional review board–approved pilot study evaluating the feasibility and dosimetric quality achieved when placing HDR prostate brachytherapy catheters with MRI guidance. The enrolled patients received two 10.5-Gy MRI-guided HDR brachytherapy boosts (21 Gy total brachytherapy dose delivered in 10.5 Gy fractions, one fraction per brachytherapy procedure) before and after a 46-Gy course of external beam radiotherapy (2 Gy/fraction), for a total of 20 implants in 10 patients. The procedures were performed with the patient in the left lateral decubitus position on a standard cylindrical 1.5T MRI scanner (Siemens Sonata; Siemens Medical Systems, Erlangen, Germany).

Details of the procedure have been previously described (25). In brief, a modified endorectal imaging coil fixed to a custom perineal template was positioned against the anterior rectal wall adjacent to the prostate gland and secured to a custom table overlay. Once optimal positioning had been obtained, an image volume encompassing the prostate gland, pubic arch, and template was acquired in a plane parallel to the template face. A peripheral catheter arrangement was generated and optimized for target coverage using a custom visualization and targeting program (26). Brachytherapy catheters (5F, 294-mm ProGuide; Nucletron, Columbia, MD) were placed and adjusted under MRI guidance until satisfactory implant geometry was achieved.

After catheter placement, final images for treatment planning were obtained, consisting of axial T_2 -weighted fast-spin-echo (FSE) images (TE 61 ms, TR 3070 ms, echo-train length (ETL) 9, pixel bandwidth (BW) 130 Hz/pixel, field of view (FOV) 15 cm, slice thickness (ST) 3 mm, 256×192 , 26 slices, number of averages (NEX) 3, scan time 6:46 min). These images were corrected for nonuniform imaging coil sensitivity and nonuniform

magnetic field gradients, geometrically reformatted for compliance to PLATO software restrictions (see below), and networked to an image server.

The corrected axial images were then loaded into the PLATO treatment planning workstation (Nucletron), and sagittal reference images were visualized (eFilm; Merge eFilm, Milwaukee, WI) on an adjacent personal computer workstation. The target volume (comprising the prostate gland and extracapsular disease), urethra, rectum, bladder, and neurovascular bundles (NVBs) were segmented. The rectum and NVBs were contoured throughout the target volume and one additional slice superiorly and inferiorly, and the urethra was defined only within the target volume.

After segmentation of the anatomy and catheters, inverse treatment planning was performed with a beta-release of an inverse planning optimization based on the simulated annealing algorithm (IPSA; Nucletron, courtesy of Jean Pouliot) (26–28). The IPSA algorithm selects active dwell positions and determines appropriate dwell times to fulfill dose constraints applied to each contoured target and organ at risk. The resulting plan delivers doses within the defined acceptable zone between the minimal and maximal dose preset for each specified organ or target. IPSA develops a solution on the basis of specified constraints within a short time (typically 30 s) and transfers the optimized dwell times to the planning system.

We performed IPSA by applying constraints to the target, urethra, bladder, and rectum with serial intuitive adjustments of dose-constraint weighting in a trial-and-error fashion until a satisfactory plan was achieved, and 1,050 cGy was prescribed to the 100% isodose. The plans obtained with this process are referred to as treated plans in this article. The plan must have achieved a target volume receiving 100% of the prescribed dose (V_{100}) of $>90\%$, a urethral volume receiving 125% of the prescribed dose (V_{125}) of $<20\%$, a rectal volume receiving 75% of the prescribed dose (V_{75}) of $<5\%$, and a bladder V_{100} of $<2 \text{ cm}^3$. An additional target margin of 2 mm was applied to account for potential error in the z dimension (see below). With the exception of the target margins, the above dose constraints were fulfilled without the use of active dwell positions outside the target to minimize normal tissue irradiation. Radiation was delivered immediately after completion of treatment planning. The brachytherapy catheters, perineal template, and endorectal coil were removed immediately after brachytherapy delivery.

Correction and verification of MR image spatial distortion

Spatial distortions on MR image are chiefly the result of non-uniform magnetic field gradients. In principle, this deviation from linearity is known for each scanner architecture and can be accurately corrected. Each image slice can be corrected for spatial distortion by applying the commercially available two-dimensional geometric correction algorithm. Phantom studies were performed to verify the accuracy of this correction.

A commercially available cylindrical water-based phantom (J3817; J.M. Specialty Parts, San Diego, CA) containing a 15-cm diameter plastic grid (1.5-cm spacing) was placed at the scanner isocenter in an oblique orientation to reproduce the clinical setup (Figs. 1e, 1f). FSE T_2 -weighted images with identical parameters to those acquired for treatment planning (see above) were obtained in a plane axial to the phantom with and without the scanner's correction for spatial distortion. The absolute distance errors were measured at 3 and 6 cm from the phantom center with medical

image processing, analysis, and visualization software (Imaging Science Laboratory, Center for Information Technology; National Institutes of Health, Bethesda, MD).

To verify that minor patient-induced spatial distortions, such as susceptibility and chemical shift distortions, did not significantly affect implant geometry in our study, noncontrast CT scans were obtained immediately after MRI and before radiation delivery in 1 patient. Treatment planning MRI and CT scans were geometrically compared using the AcQSIM 3D treatment planning software package on a VoxelQ workstation (Picker) with CT–MRI rigid reference point registration (29). Concordance of catheter and organ location throughout the target volume was thereby subjectively evaluated (Fig. 1).

DICOM header correction for compliance to treatment planning software

To maximize the accuracy of catheter digitization and anatomic visualization during MRI-guided brachytherapy procedures, treatment planning MRIs were acquired in equally spaced slices parallel to the plane of the template. Because the brachytherapy treatment planning software will only accept true axial image sets acquired perpendicular to the direction of couch travel, corrections to the DICOM header in the raw image data were applied to permit image transfer into PLATO.

To obtain the desired planning image orientation and slice thickness in planes parallel to the perineal template, two data elements in the DICOM header of each MRI planning study were modified (tags of [0x0020, 0x0032] and [0x0020, 0x0037]). These two DICOM image header tags corresponded to the position and orientation of the images, respectively. The position element was modified based on slice number, in which the position element of the i -th image slice was modified to be $[x1, y1, z1 + (i - 1) * \text{thickness}]$, $i \geq 1$, and the orientation element changed to be $[(1, 0, 0) \times (0, 1, 0)]$. These descriptive parameter changes allowed coordinate transformation from the scanner coordinate (slices along the longitudinal axis of the couch) to the template rectal coordinate (along the longitudinal rectal probe axis, perpendicular to the perineal template). These corrections were then tested with

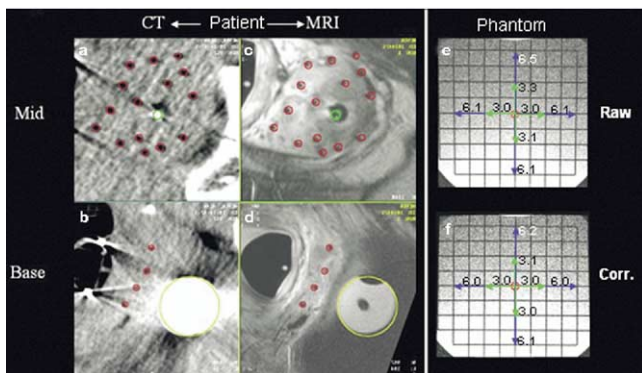


Fig. 1. (a–d) Treatment planning magnetic resonance imaging (MRI) and postimplant computed tomography (CT) fusion in 1 patient. Rigid reference point fusion of treatment planning MRI and postimplant CT images confirmed lack of measurable image distortion in x - y plane because of patient-related chemical shift or susceptibility. Absolute spatial error was measured in grid phantom with 1.5-cm spacing (e) before and (f) after correction for spatial distortion because of gradient nonlinearity.

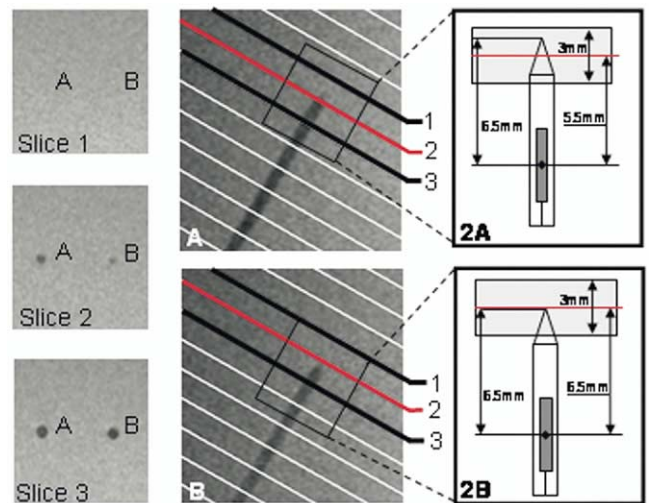


Fig. 2. Evaluation of catheter visibility. Brachytherapy catheters embedded in phantom material were imaged at varying depths beyond slice center to evaluate the effects of volume averaging and catheter tip depth on tip visibility. Catheter A was advanced 1 mm beyond the center of slice 2 (red line). Catheter A was clearly visible on slices 2 and 3 and not visible on slice 1 (left panel). Catheter B was advanced to the exact center of slice 2 (red line), was barely visible on slice 2, and was well visualized on slice 3 but not slice 1 (left panel). Distance from source center at first dwell position (diamond) to slice center was 5.5 mm for catheter A (right upper corner) and 6.5 mm for catheter B (right lower corner). Catheter B represents largest distance between slice center of visualized tip and physical location of first dwell position.

phantom measurements to verify appropriate orientation and spatial integrity.

A custom $20 \times 20 \times 10$ -cm water phantom with four 5F catheters fitted through four parallel holes arranged in a 10×10 -cm square was built for this experiment. Two MRI scans were acquired with the phantom first placed in an oblique orientation to the scanner bore, which reproduced the clinical catheter orientation and treatment planning images (see above) acquired in an axial plane to the catheters. The phantom was then rotated 90° , and the treatment planning image sequence was repeated. The first and second MRI acquisitions were used to verify the axial and sagittal image spatial integrity, respectively, after header tag correction and transfer into PLATO.

Determination of first dwell position

Determination of the location of the first dwell position based on visualization of the signal void at the needle tip was verified in a 1 L gelatin phantom. Six plastic catheters with their metal obturators (5F Proguide; Nucletron) were inserted as pairs to depths of 80, 81, and 82 mm. The catheters were placed in a single plane with a center-to-center spacing of 5 mm. After insertion of the catheters, the perineal template locking mechanism was used, and the template was secured to the gelatin phantom container. Obturators were removed before imaging as per standard procedure. FSE T_2 -weighted images with acquisition parameters identical to the treatment planning images were obtained in the axial and sagittal planes relative to the catheters. Catheter tip visualization on axial images was compared against sagittal reference to slice center (Fig. 2).

Evaluation of anatomy based on MRI

In addition to T₂-weighted FSE axial images of the prostate gland, the following two image sequences were acquired to aid in anatomic delineation. First, images of the NVBs were acquired shortly after intravenous administration of 0.1 mmol/kg gadolinium chelate and before catheter placement (3D TrueFISP 4.7/2.4 ms TR/TE, 1.5 mm thick, matrix 256 × 256, 20 × 20 field of view, imaging time 1:58 min). In some instances, NVB images were used to alter catheter placement. Second, to improve definition of the superoinferior extent and relationship of the target relative to normal structures, sagittal T₂-weighted FSE images were acquired (TE 121 ms, TR 3,500 ms, echo-train length 9, field of view 25 cm, ST = 3 mm, slices 20, scan time 3:28 min) after catheter placement and before treatment planning. The MRI data were used to evaluate unique anatomic variables, including prostate organ shift in left lateral decubitus position, the distance from the prostate apex to the penile bulb, and the location and path of the NVBs relative to the prostate gland. Prostate deviation from midline in the left lateral decubitus position was measured by determining the distance between the center of the urethra and midline of the bony pelvis on axial MRI.

Derivation of class solution for inverse planning constraints

Treatment planning MRI data from 10 patients were used to determine a class solution of optimal inverse planning constraints. Determination of the optimal constraints was performed by systematically evaluating the effects of increasing the “weight” on the upper and lower dose constraints for each target and critical normal tissue. Minimal and maximal dose limits were determined on the basis of levels considered clinically acceptable (30, 31). For example, the lower dose limit for the target was the prescribed dose (1,050 cGy), and the upper dose constraint was 150% (1,575 cGy) of the prescription dose (V_{150}). The upper rectal dose constraint was 75% of the prescribed dose (787.5 cGy), and the urethral upper dose constraint was 125% of the prescribed dose (1,312.5 cGy).

Determination of optimal target dose constraint weighting was followed by the sequential determination of the optimal dose constraint weights for each normal tissue in order of relative clinical importance. The maximal achievable target coverage was determined by applying maximal weight to the prescription dose (lower dose constraint) and zero weight to the maximal dose constraint of the target and all normal tissue dose goals. The target upper dose constraint weight was incrementally increased to determine the optimal weight required to minimize heterogeneity within the implant while maintaining adequate target coverage. Critical organs were then sequentially added into the planning algorithm to determine the optimal constraints for each organ.

After determination of the optimal target constraints, the optimal constraint weights for the urethral volume were determined. On the basis of the intraprostatic location of the urethra, we hypothesized a more significant effect on target dosimetry with application of a minimal dose goal to this structure as a result of reduced periurethral target “cold spots.” For this reason, the minimal and maximal dose constraint weights were serially modulated to determine their effect on urethral and target dosimetry. For all other nontarget tissues located outside the target, only the maximal dose constraint weights were evaluated. After determination of the optimal target and urethral constraints, the rectal, bladder, and NVB optimal constraints were derived, in that order.

The final target and normal tissue dosimetry achieved with this class solution was compared with the dosimetry of the delivered treatment plans in which the dose constraints were intuitively adjusted to meet predetermined dose goals. The dosimetry obtained with target dose constraints alone (i.e., maximal achievable target coverage) was also compared with the dosimetry achieved with the class solution to determine the efficiency of the class solution. The decrement in target V_{100} with the addition of each normal tissue to the planning algorithm was determined to evaluate the relative importance of each tissue on target dosimetry.

RESULTS

Correction and verification of MRI spatial distortion

Phantom measurements confirmed the accuracy of the correction applied to the MRI scans to account for spatial distortion (Figs. 1e, 1f). Distance measurements from the isocenter found near perfect agreement to the true physical distance of the phantom at 3 cm and a 1–2 mm error in the y dimension at 6 cm from the isocenter. Treatment planning MRI and postimplant CT fusion confirmed a lack of measurable image distortion due to patient-related chemical shift or susceptibility artifact (Figs. 1a–d).

DICOM header correction for compliance to treatment planning software

Phantom measurements verified spatial integrity of MRI after header correction. The distances between the four catheters measured on PLATO were 100 mm and 100.7 mm in the y dimension, 99.6 and 99.5 mm in the x dimension, and 102.0 mm in the z dimension. The 2-mm error measured in the z dimension was attributed to either uncorrected MRI spatial distortion in the z dimension or a volume average of the 3-mm slice. Each slice accurately reflected the known 3-mm slice thickness in PLATO. These results confirmed the validity of our header correction method.

Determination of first dwell position

The physical distance between the tip of the catheter and the first dwell position was measured at 6.5 mm on our system. MRI of catheters embedded in phantom material revealed an accurate ability to determine the location of the first dwell position using visualization of the catheter tip on the axial images. The maximal distance from the slice center of the visualized tip (Fig. 2, slice 2) to the first dwell position was 6.5 mm (slice 2 of catheter B, Fig. 2). Owing to volume averaging in our 3-mm slice thickness, the minimal distance between the visualized tip and the first dwell position was determined to be 5 mm. The optimal offset from the visualized catheter tip on 3-mm-thick axial MR phantom images to the first dwell position was therefore 5.75 mm, with an error of ±0.75 mm. Because our treatment planning software will not accept submillimeter offsets, we chose to place an offset of 6 mm from the digitized catheter tip to identify the location of the first dwell position for each catheter in the image set. We estimated this approach to yield an error of ±1 mm.

Evaluation of anatomy based on MRI

Deviation of the prostate gland in the left lateral decubitus position was measured as the lateral distance between the urethra and the middle of the symphysis pubis (Fig. 3a). The mean prostate deviation from midline was 1.47 mm (range, 5 mm left shift to 6 mm right shift). In 7 of 20 implants, no deviation of the prostate from the midline was measured. The mean prostate apex to penile bulb distance was 14.47 mm (range, 2–29). On the basis of the magnitude of this distance and the rapid dose falloff with HDR brachytherapy, a penile bulb constraint was not included in the inverse planning optimization.

As described above, the NVBs can be effectively visualized on MRI during this procedure. The typical course of the NVBs can be appreciated in Fig. 4. The right and left NVBs coursed along the posterolateral border of the prostate gland and moved medially and anteriorly at the apex of the prostate. With a transperineal approach, they were positioned between the perineal template and prostate gland directly in the path of the brachytherapy catheters. Visualization of the NVBs may allow avoidance of these structures during the brachytherapy procedure when anatomically feasible.

Another benefit of real-time MRI guidance for brachytherapy is the ability to visualize and target extraprostatic disease extension. In all patients, lesions suspicious for malignancy could be identified. In 2 patients, extraprostatic extension was visualized and specifically targeted with catheter placement, with inclusion in the contoured target volume. In 1 patient, accurate visualization of a utricular cyst (Fig. 3) allowed implantation with excellent target dosimetry and without puncture of the cyst (target V_{100} , 94.4% and 93.9%).

Determination of class solution for inverse planning constraints

The target dose constraint weighting that resulted in maximal target coverage with acceptable V_{150} resulted in a mean target V_{100} of 98.10% (range, 96.44–99.57%), with a mean target V_{150} of 46.24% (range, 38.95–54.38%). A rapid decrease in the target V_{150} was achieved with an increase in the upper dose constraint weight from 0 to 10 (on a scale of

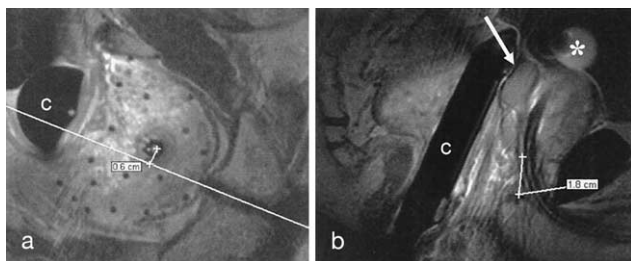


Fig. 3. Evaluation of anatomy. (a) Measurement of prostate shift in left lateral decubitus position was accomplished by evaluating shift of urethra relative to bony pelvis. (b) Penile bulb to prostatic apex distance was measured on sagittal magnetic resonance imaging. Note that patient's utricular cyst (asterisk) was clearly visible on magnetic resonance imaging. C = endorectal coil.

0–100; Fig. 5a). Additional increases in the target maximal dose constraint weight resulted in minimal improvements in the target V_{150} with a substantial decrease in the target V_{100} . For these reasons, a target maximal dose constraint weight of 10 was selected as optimal.

Evaluation of the urethral upper and lower dose constraint weights revealed optimal target coverage with an acceptable urethral V_{125} when lower dose constraint weights were given moderate weighting, with maximal weight placed on the upper dose limits (Fig. 5b). Increasing the weight on the minimal dose limit (i.e., increasing the importance placed on the urethra achieving at least the minimal dose), resulted in improved target dosimetry, decreasing periurethral target “cold spots.” Increasing the weight on the urethral upper dose limits decreased the urethral V_{125} and minimally decreased the target V_{100} . A urethral lower dose constraint weight of 20 (scale 0–100) and urethral upper dose constraint weight of 100 (scale 0–100) were determined to deliver the best target dosimetry while resulting in a urethral V_{125} of <2% in all cases evaluated. The selected urethral weighting, combined with the previously defined target weighting, resulted in a mean target V_{100} of 96.08% (range, 91.52–98.41%), with a mean urethral V_{125} of 0.54% (range, 0.08–2.28%).

The addition of rectal maximal dose constraint weighting resulted in a minimal decrement in target coverage (Fig. 5c). A rectal upper dose constraint weight of 30 was the lowest weight capable of achieving a rectal V_{75} of <5% for all evaluated cases. In cases in which the rectal dose goals were achieved at weights of <30, increasing the weight to 30 did not significantly decrease the target dosimetry. On the basis of these results, a rectal upper dose constraint weight of 30 was determined to be optimal, resulting in a mean rectal V_{75} of 1.36%.

In all cases, the volume of bladder receiving the prescription dose was <2 cm³ (mean, 0.55), thus requiring no weight (0, scale 0–100) on the bladder maximal dose limit. The addition of a maximal dose constraint weight to the NVBs of 10 (scale 0–100) resulted in an additional minimal decrement in the target V_{100} and resulted in 0% of the NVB receiving 125% of the prescribed dose (Fig. 5c).

The class solution appeared to be efficient and effective, achieving all normal tissue dose goals with minimal decrement to the maximally achievable target V_{100} . The initial target V_{100} with maximal weight placed on achieving lower dose goals without regard to target V_{150} resulted in a target V_{100} of 100% (Fig. 5d, target a). The addition of an upper dose constraint weight that resulted in acceptable target V_{150} produced a mean target V_{100} of 98.10% (Fig. 5d, target b). Overall, the addition of the urethral, rectal, bladder, and NVB dose constraints resulted in a mean decrement of 2.89% (range, 0.45–5.02%) in the target V_{100} compared with optimization of the target without the critical structures taken into account. The class solution improved target dosimetry in all patients evaluated compared with the treated plans (Fig. 5d). The mean target V_{100} achieved with the treated plans

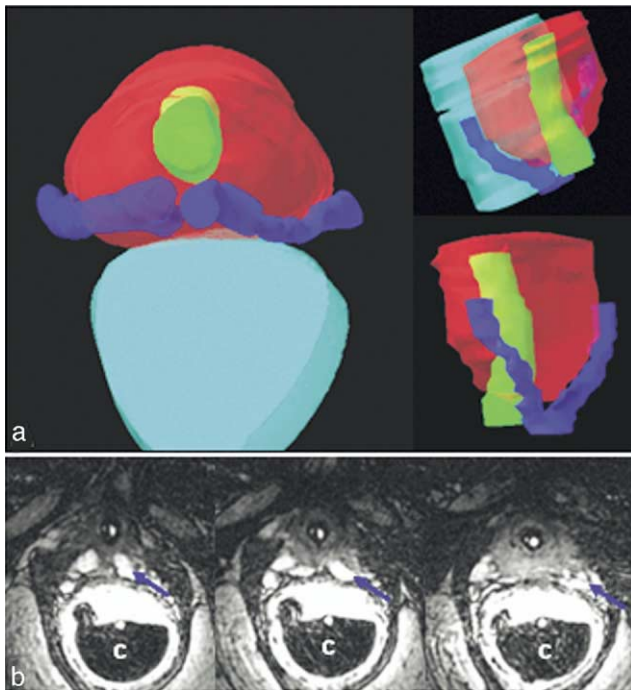


Fig. 4. Neurovascular bundles (NVB) imaging. (a) Three-dimensional (3D) reconstruction of course of NVB (blue) along prostate gland (red) based on (b) postcontrast 3D TrueFISP images. Left figure represents 3D view of anatomy from perineum. Note that transperineal catheter placement into peripheral zone impinges on NVBs.

was 92.97% (range, 86.6–95.82%), and the mean target V_{100} achieved with the class solution was 95.69% (range, 90.61–98.36%). A comparison of dosimetric results obtained with the class solution and treated plans is presented in Table 1.

DISCUSSION

Magnetic resonance imaging has been evaluated for use in many aspects of prostate brachytherapy from staging and patient selection to treatment planning. MRI is a highly sensitive tool for detecting the presence of extraprostatic disease extension (32), potentially altering treatment recommendations (21). MRI has also been used to evaluate postimplant seed distributions (18).

Recently, MRI has played an important role in the treatment planning for brachytherapy and during the brachytherapy procedure. As discussed above, all previous studies evaluating MRI for treatment planning and delivery for prostate cancer have used deformable object-based image registration to link MRI to CT scans for treatment planning. Deformable registration is required in this setting to account for alterations in the shape of the prostate and normal surrounding structures that occur in the interval between obtaining the reference image set and the secondary (MRI) image set. Deformations in the prostate and surrounding organs and tissues may result from the physiologic variabil-

ity in bladder and rectal filling, positional changes, or insertion of an endorectal coil to obtain the MRI scans.

The spatial transformation of the secondary image set required in deformable registration introduces geometric and spatial uncertainties, resulting in a decrement in secondary image quality. The magnitude of this decrement is dictated by the amount of deformation and reformatting required to perform an accurate fusion to the reference image, which may be large if significant prostate deformation occurs between acquisition of the two image sets. Using MRI as the reference image without registration bypasses the need for deformation and the resultant decrement in image quality and spatial integrity. The ability to maintain the patient in the left lateral decubitus position with template and endorectal coil in place in our procedure allowed the use of planning MRI as the reference image without the need for image fusion, thus eliminating the inaccuracies inherent in deformable registration.

The development of MRI-guided HDR prostate brachytherapy at our institution mandated a systematic and thorough evaluation of the spatial accuracy of the planning images and the effects of volume averaging. Brachytherapy planning requires accuracy within millimeters to determine the delivered dose, requiring high-spatial accuracy of the planning images. After applying a correction, phantom images were found to be spatially accurate in the x - y plane. The evaluation of MRI planning data from a treated patient confirmed the spatial integrity. Note that our results are

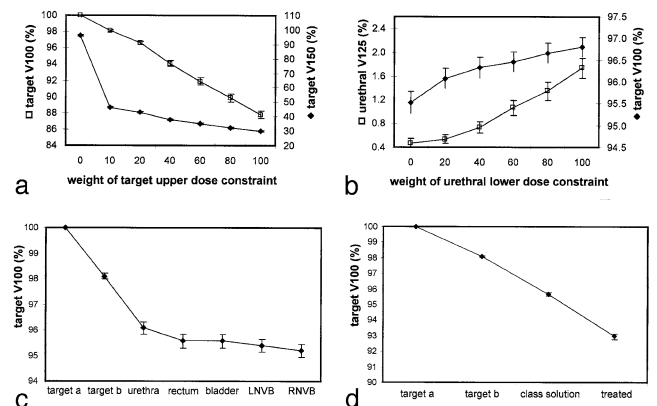


Fig. 5. Inverse planning constraint optimization. (a) Target optimization. Target V_{150} decreased rapidly with addition of small weight on upper target dose constraints, and target V_{100} decreased at slower rate. (b) Urethral optimization. Increasing weight on urethral lower dose constraint improved target dosimetry markedly and increased urethral V_{125} minimally. (c) Effect of sequential normal tissue optimization on target dosimetry. Target a = maximal achievable heterogeneous target V_{100} (no weight on target upper dose constraint); target b = maximal achievable homogeneous target V_{100} (weight applied to target upper dose constraint); NVB = neurovascular bundles; LNVB = left NVB; RNVB = right NVB. (d) Decrease in target V_{100} with addition of target upper dose constraint weight (target b) and normal tissue dose constraints (class solution). Class solution resulted in superior target V_{100} compared with treated plans.

Table 1. Comparison of dosimetric parameters

Dosimetric parameters	Treated plans (%)	Class solution (%)	<i>p</i>
Target V_{100}	92.97	95.69	0.03
Urethral V_{125}	4.78	0.54	0.02
Rectal V_{75}	1.41	1.36	0.40
Bladder V_{100}	0.17	0.22	0.43
LNVB V_{125}	0.02	0.00	0.03
RNVB	0.01	0.00	0.04

Abbreviations: LNVB = left neurovascular bundle; RNVB = right NVB; V_{75} = volume receiving 75% of prescribed dose; V_{100} = volume receiving 100% of prescribed dose; V_{125} = volume receiving 125% of prescribed dose.

limited to correction and verification in the x–y plane. To our knowledge, no correction algorithms are commercially available for the slice-select z dimension. Although we anticipate this error to be small, additional work will address this issue.

A second source of error in the z axis stems from 3-mm slice volume averaging. Although this may affect target delineation, offline sagittal image reference may have reduced this potential error. We plan to evaluate the feasibility of obtaining planning images with 1.5-mm slice thickness images to reduce z axis uncertainty due to volume averaging. Reducing the slice thickness will require a second evaluation of the catheter visibility to determine whether the decreased slice thickness will alter the magnitude of catheter position error.

In the same vein, a rigorous determination of the ability to detect catheters at varying depths within an MRI slice allowed confidence regarding the appropriate offset at which to determine the location of the first dwell position. A limitation of this approach is the inability to define the catheter tip, target, and critical tissues with less than ± 1 mm of accuracy in the z axis because of slice-thickness volume averaging. Finally, a third source of potential error in this dimension relates to catheter displacement relative to the prostate between image acquisition and radiation delivery. Combined, these sources of inaccuracy can be addressed by minimally increasing the margin placed on the target in this dimension. Although at the outset of the study we chose to adopt a target margin of 2 mm in the z dimension, this margin has now been increased to 3 mm pending further work to define this error better.

In our procedure, all images were obtained and all treatments delivered with the patient in the left lateral decubitus position. During the development of the procedure, concern was raised that positioning the patient in the left lateral decubitus position might result in a shift of the gland to the left side of the pelvis, resulting in an inability to implant the gland adequately with brachytherapy catheters. Evaluation of prostate deviation from the midline in this position revealed no reproducible systemic offset from the midline. In several cases, the prostate deviated visibly to the right and left of midline; however, the mean displacement from midline was 0 mm. It is

unclear whether the prostate shifted from its baseline position, because we did not determine the amount of shift that occurred when repositioning from supine or prone to the left lateral decubitus position. Nonetheless, on the basis of our measurements, the left lateral decubitus position appears suitable for brachytherapy implantation with regard to prostate deviation from midline.

Previous studies have found substantial intraobserver and interobserver variability with the use of CT to define the prostate volume (33–36). MRI has been shown to significantly reduce interobserver and intraobserver variability in prostate delineation for brachytherapy compared with CT (33). We believe that the quality of anatomic visualization with MRI guidance may have improved our accuracy in delineating the target and critical structures.

MRI has been used to determine the doses to erectile tissues after prostate brachytherapy (37). Altering prostate brachytherapy procedures to minimize the dose to areas at which the NVBs characteristically reside was also recently described (38). The effect of this dose reduction remains controversial (38–43). In our study, we were able to visualize the NVBs directly during the implantation of the catheters and the treatment planning process. This afforded an opportunity to minimize both needle traumatic injury and radiation injury during HDR brachytherapy, which may translate into lower morbidity.

Our goal was to define a set of planning constraints that resulted in acceptable target and normal tissue dosimetry in all patients undergoing this procedure. The development of a class solution for inverse planning constraints for our procedure resulted in improved target dosimetry and normal tissue sparing compared with plans obtained before these constraints were introduced. The development of a class solution has the potential to reduce the time required for treatment planning, an important consideration in our protocol.

In our evaluation of dose constraint weights, we chose to evaluate weights in steps of 5 on a scale of 0–100. Although a large number of possible combinations of dose constraint weights were evaluated, it is possible that another solution exists that provides similar or slightly improved target and normal tissue dosimetry. It is also reasonable to consider that improvement in the dosimetry of one organ may effect the optimal weighting of a second organ, thus requiring a near infinite number of iterations to achieve the optimal solution. In our study, the dosimetric results obtained with the class solution did not appear to be different from those obtained during the sequential addition of structures to the planning algorithm (i.e., the addition of other organs did not affect normal tissue dosimetry appreciably). The exception to this statement is the target dosimetry, which suffered a decrement in the V_{100} with the addition of each organ to the algorithm. Conversely, the addition of a second normal tissue improved the dosimetry of the first in some cases, such as in the addition of the NVBs to the planning algorithm, which further decreased the rectal dose in a

subset of patients. We are hopeful that this systematic approach for developing an inverse planning class solution can be applied to other procedures requiring inverse planning.

The ability to use high-quality MRI for treatment planning allows a precise definition of target and normal tissues using anatomic boundaries. Additional refinements in targeting will now be possible by adapting this technique to incorporate functional and biologic imaging. By localizing the intraprostatic tumor volume (44, 45), spectroscopic MRI and dynamic contrast-enhanced MRI may help to define areas within the target that may benefit from local dose escalation with our procedure.

CONCLUSIONS

Inverse planning for MRI-guided HDR prostate brachytherapy requires confidence in the spatial integrity of the planning images, including the accuracy of catheter location

and anatomic definition. A systematic evaluation of the spatial integrity and delineation uncertainty for our MRI-guided HDR prostate brachytherapy procedure was performed, confirming the spatial and targeting accuracy. Verification of multiple technical aspects of the treatment planning MRI and planning process will allow a reduction in the uncertainty in targeting, planning, and treatment delivery.

The development of a class solution for inverse planning dose constraints for target and normal tissue has provided a helpful tool when performing our brachytherapy procedure, potentially decreasing the time required to achieve acceptable dosimetry. In our experience, the class solution we developed for our procedure is effective at achieving excellent target dosimetry while sparing nearby normal tissues. Furthermore, the technique we used to determine the optimal inverse planning constraints can likely be applied to other brachytherapy procedures and treatments involving inverse planning.

REFERENCES

1. Nguyen PL, Whittington R, Koo S, *et al.* Quantifying the impact of seminal vesicle invasion identified using endorectal magnetic resonance imaging on PSA outcome after radiation therapy for patients with clinically localized prostate cancer. *Int J Radiat Oncol Biol Phys* 2004;59:400–405.
2. Cheng GC, Chen MH, Whittington R, *et al.* Clinical utility of endorectal MRI in determining PSA outcome for patients with biopsy Gleason score 7, PSA \leq 10, and clinically localized prostate cancer. *Int J Radiat Oncol Biol Phys* 2003;55:64–70.
3. D'Amico AV, Whittington R, Malkowicz SB, *et al.* Combination of the preoperative PSA level, biopsy Gleason score, percentage of positive biopsies, and MRI T-stage to predict early PSA failure in men with clinically localized prostate cancer. *Urology* 2000;55:572–577.
4. D'Amico AV, Schnall M, Whittington R, *et al.* Endorectal coil magnetic resonance imaging identifies locally advanced prostate cancer in select patients with clinically localized disease. *Urology* 1998;51:449–454.
5. D'Amico AV, Whittington R, Malkowicz SB, *et al.* Combined modality staging of prostate carcinoma and its utility in predicting pathologic stage and postoperative prostate specific antigen failure. *Urology* 1997;49:23–30.
6. D'Amico AV, Whittington R, Malkowicz SB, *et al.* Role of percent positive biopsies and endorectal coil MRI in predicting prognosis in intermediate-risk prostate cancer patients. *Cancer J Sci Am* 1996;2:343.
7. D'Amico AV. The role of MR imaging in the selection of therapy for prostate cancer. *Magn Reson Imag Clin North Am* 1996;4:471–479.
8. D'Amico AV, Whittington R, Schnall M, *et al.* The impact of the inclusion of endorectal coil magnetic resonance imaging in a multivariate analysis to predict clinically unsuspected extraprostatic cancer. *Cancer* 1995;75:2368–2372.
9. Hasumi M, Suzuki K, Oya N, *et al.* MR spectroscopy as a reliable diagnostic tool for localization of prostate cancer. *Anticancer Res* 2002;22:1205–1208.
10. Coakley FV, Kurhanewicz J, Lu Y, *et al.* Prostate cancer tumor volume: Measurement with endorectal MR and MR spectroscopic imaging. *Radiology* 2002;223:91–97.
11. Scheidler J, Hricak H, Vigneron DB, *et al.* Prostate cancer: localization with three-dimensional proton MR spectroscopic imaging—Clinicopathologic study. *Radiology* 1999;213:473–480.
12. Ito H, Kamoi K, Yokoyama K, *et al.* Visualization of prostate cancer using dynamic contrast-enhanced MRI: Comparison with transrectal power Doppler ultrasound. *Br J Radiol* 2003;76:617–624.
13. Mizowaki T, Cohen GN, Fung AY, *et al.* Towards integrating functional imaging in the treatment of prostate cancer with radiation: the registration of the MR spectroscopy imaging to ultrasound/CT images and its implementation in treatment planning. *Int J Radiat Oncol Biol Phys* 2002;54:1558–1564.
14. Wu X, Dibiase SJ, Gullapalli R, *et al.* Deformable image registration for the use of magnetic resonance spectroscopy in prostate treatment planning. *Int J Radiat Oncol Biol Phys* 2004;58:1577–1583.
15. Sannazzari GL, Ragona R, Ruo Redda MG, *et al.* CT-MRI image fusion for delineation of volumes in three-dimensional conformal radiation therapy in the treatment of localized prostate cancer. *Br J Radiol* 2002;75:603–607.
16. Buyyounouski MK, Horwitz EM, Price RA, *et al.* Intensity-modulated radiotherapy with MRI simulation to reduce doses received by erectile tissue during prostate cancer treatment. *Int J Radiat Oncol Biol Phys* 2004;58:743–749.
17. Steenbakkens RJ, Deurloo KE, Nowak PJ, *et al.* Reduction of dose delivered to the rectum and bulb of the penis using MRI delineation for radiotherapy of the prostate. *Int J Radiat Oncol Biol Phys* 2003;57:1269–1279.
18. Coakley FV, Hricak H, Wefer AE, *et al.* Brachytherapy for prostate cancer: Endorectal MR imaging of local treatment-related changes. *Radiology* 2001;219:817–821.
19. Krempien RC, Daeuber S, Hensley FW, *et al.* Image fusion of CT and MRI data enables improved target volume definition in 3D-brachytherapy treatment planning. *Brachytherapy* 2003;2:164–171.
20. Pouliot J, Kim Y, Lessard E, *et al.* Inverse planning for HDR prostate brachytherapy used to boost dominant intraprostatic lesions defined by magnetic resonance spectroscopy imaging. *Int J Radiat Oncol Biol Phys* 2004;59:1196–1207.
21. Clarke DH, Banks SJ, Wiederhorn AR, *et al.* The role of endorectal coil MRI in patient selection and treatment plan-

- ning for prostate seed implants. *Int J Radiat Oncol Biol Phys* 2002;52:903–910.
22. DiBiase SJ, Hosseinzadeh K, Gullapalli RP, *et al.* Magnetic resonance spectroscopic imaging-guided brachytherapy for localized prostate cancer. *Int J Radiat Oncol Biol Phys* 2002; 52:429–438.
 23. D'Amico A, Cormack R, Kumar S, *et al.* Real-time magnetic resonance imaging-guided brachytherapy in the treatment of selected patients with clinically localized prostate cancer. *J Endourol* 2000;14:367–370.
 24. Susil RC, Camphausen K, Choyke P, *et al.* System for prostate brachytherapy and biopsy in a standard 1.5 T MRI scanner. *Magn Reson Med* 2004;52:683–687.
 25. Ménard C, Susil RC, Choyke P, *et al.* MRI-guided HDR prostate brachytherapy in a standard 1.5T scanner. *Int J Radiat Oncol Biol Phys* 2004;59:1414–1423.
 26. Lessard E, Pouliot J. Inverse planning anatomy-based dose optimization for HDR-brachytherapy of the prostate using fast simulated annealing algorithm and dedicated objective function. *Med Phys* 2001;28:773–779.
 27. Lessard E, Hsu IC, Pouliot J. Inverse planning for interstitial gynecologic template brachytherapy: Truly anatomy-based planning. *Int J Radiat Oncol Biol Phys* 2002;54:1243–1251.
 28. Lachance B, Beliveau-Nadeau D, Lessard E, *et al.* Early clinical experience with anatomy-based inverse planning dose optimization for high-dose-rate boost of the prostate. *Int J Radiat Oncol Biol Phys* 2002;54:86–100.
 29. Lau H, Kagawa K, Lee W, *et al.* Short communication: CT-MRI image fusion for 3D conformal prostate radiotherapy—Use in patients with altered pelvic anatomy. *Br J Radiol* 1996;69:1165–1170.
 30. Martinez AA, Gustafson G, Gonzalez J, *et al.* Dose escalation using conformal high-dose-rate brachytherapy improves outcome in unfavorable prostate cancer. *Int J Radiat Oncol Biol Phys* 2002;53:316–327.
 31. Rodriguez RR, Demanes DJ, Altieri GA. High dose rate brachytherapy in the treatment of prostate cancer. *Hematol Oncol Clin North Am* 1999;13:503–523.
 32. Bernstein MR, Cangiano T, D'Amico A, *et al.* Endorectal coil magnetic resonance imaging and clinicopathologic findings in T1c adenocarcinoma of the prostate. 2000;5:104–107.
 33. Dubois DF, Prestidge BR, Hotchkiss LA, *et al.* Intraobserver and interobserver variability of MR imaging- and CT-derived prostate volumes after transperineal interstitial permanent prostate brachytherapy. *Radiology* 1998;207:785–789.
 34. Fiorino C, Reni M, Bolognesi A, *et al.* Intra- and interobserver variability in contouring prostate and seminal vesicles: Implications for conformal treatment planning. *Radiation Oncol* 1998;47:285–292.
 35. Berthelet E, Liu MC, Agranovich A, *et al.* Computed tomography determination of prostate volume and maximum dimensions: A study of interobserver variability. *Radiation Oncol* 2002;63:37–40.
 36. Han BH, Wallner K, Merrick G, *et al.* The effect of interobserver differences in post-implant prostate CT image interpretation on dosimetric parameters. *Med Phys* 2003;30:1096–1102.
 37. Buyyounouski MK, Horwitz EM, Uzzo RG, *et al.* The radiation doses to erectile tissues defined with magnetic resonance imaging after intensity-modulated radiation therapy or iodine-125 brachytherapy. *Int J Radiat Oncol Biol Phys* 2004;59: 1383–1391.
 38. Wright JL, Newhouse JH, Laguna JL, *et al.* Localization of neurovascular bundles on pelvic CT and evaluation of radiation dose to structures putatively involved in erectile dysfunction after prostate brachytherapy. *Int J Radiat Oncol Biol Phys* 2004;59:426–435.
 39. Merrick GS, Butler WM. The dosimetry of brachytherapy-induced erectile dysfunction. *Med Dosim* 2003;28:271–274.
 40. Merrick GS, Butler WM, Dorsey AT, *et al.* A comparison of radiation dose to the neurovascular bundles in men with and without prostate brachytherapy-induced erectile dysfunction. *Int J Radiat Oncol Biol Phys* 2000;48:1069–1074.
 41. Kiteley RA, Lee WR, deGuzman AF, *et al.* Radiation dose to the neurovascular bundles or penile bulb does not predict erectile dysfunction after prostate brachytherapy. *Brachytherapy* 2002;1:90–94.
 42. DiBiase SJ, Wallner K, Tralins K, *et al.* Brachytherapy radiation doses to the neurovascular bundles. *Int J Radiat Oncol Biol Phys* 2000;46:1301–1307.
 43. Bradley KA, Chappell R, Yuan Z, *et al.* Erectile dysfunction and prostate brachytherapy doses to the penile bulb and neurovascular bundles. *Int J Radiat Oncol Biol Phys* 2003;57: S399–S400.
 44. Schlemmer HP, Corvin S. Methods for volume assessment of prostate cancer. *Eur Radiol* 2004;14:597–606.
 45. Kurhanewicz J, Vigneron DB, Hricak H, *et al.* Three-dimensional H-1 MR spectroscopic imaging of the in situ human prostate with high (0.24–0.7-cm³) spatial resolution. *Radiology* 1996;198:795–805.